The Effect of Ambient Pressure on Flame Spread Over Thin Cellulosic Fuel in a Quiescent, Microgravity Environment

S. Bhattacharjee
Department of Mechanical Engineering,
San Diego State University,
San Diego, CA 92182

R. A. Altenkirch
Department of Mechanical Engineering and
NSF Engineering Research Center for
Computational Field Simulation,
Mississippi State University,
Mississippi State, MS 39762

K. Sacksteder
NASA Lewis Research Center,
Cleveland, OH 44135

Results from recently conducted experiments on flame spread over a thin cellulosic fuel in a quiescent, microgravity environment of a 50/50 volumetric mixture of oxygen and nitrogen (oxygen mass fraction 0.53) at three different pressures—101, 152, and 203 kPa (1, 1.5, and 2.0 atm)—are analyzed. The results are compared with established theoretical results and two different computational flame spread models: one that includes gas-phase radiation, and one that does not. The spread rate behavior from experiment, i.e., an increase of spread rate with pressure, is consistent with the theoretical model that includes gas-phase radiation, and side-view photographs of the flames compare favorably with two-dimensional temperature contours produced computationally from the same model. In contrast, neither the dependence of spread rate on pressure nor the flame shape can be predicted with favorable comparison to experiment if radiation is neglected.

Introduction

The effect of ambient pressure on flame spread over thermally thin fuels in a normal-gravity environment is well known (Altenkirch and Bhattacharjee, 1990; Lastrina et al., 1971; Williams, 1976; de Ris, 1969) and can be deduced from simple scaling arguments. However, in a microgravity environment, complications arise because the conduction length scale based on a balance of upstream heat conduction and downstream convection, appropriate for flame spread into an opposing flow, becomes larger than the actual physical scale of the flame due to lack of any buoyancy-induced flow.

Consider the opposed-flow configuration depicting flame spread over a thin fuel shown in Fig. 1. In flame-fixed coordinates the oxidizer approaches with a velocity $V_r = V_f + V_g$, and the solid fuel approaches the flame with a velocity V_f, a desired unknown. Because heat transfer ahead of the flame leading edge constitutes the mechanism of flame spread, the length over which heat is transferred at the leading edge is important for scaling purposes. The balance between forward heat conduction and convection at the flame leading edge produces a thermal length scale of $L_g = \alpha_g/V_r$, also a diffusion length scale for unit Lewis number. For thin solids ($\tau \ll L_g$), gas-phase conduction is the principal forward heat transfer mechanism ahead of the flame if radiation is neglected, so L_g is the characteristic length scale for the entire problem.

The simplest model of flame spread is the thermal model in which a thin solid fuel of half-thickness τ is heated from T_∞ to a vaporization temperature T_v by conduction heat transfer from the flame to the fuel ahead of it (the preheat zone). In approximate terms, the conductive flux is $\dot{q}''_{gsc} \approx \lambda_g(T_f - T_v)/L_g$, and the length of the preheat zone is L_g, so that the total heat transfer rate is approximately $\lambda_g(T_f - T_v)$. This forward heat transfer is responsible for the sensible heating of the fuel moving at a speed V_f toward the flame, the rate of heating being $\rho_s\tau C_s V_f(T_v - T_\infty)$. Balancing these rates, $V_f \approx (\lambda_g/\tau\rho_s C_s)(T_f - T_v)/(T_v - T_\infty)$, which is similar in form to the classical solution of the flame spread problem developed by de Ris (1969). According to this expression, for fixed T_f, which for fixed $m_{ox,\infty}$ obtains for infinitely fast gas-phase kinetics, the spread rate is independent of pressure and opposing flow velocity provided the vaporization temperature, T_v, known experimentally or from correlation (Bhattacharjee et al., 1994a, b) is independent of pressure. The conduction length scale, L_g, is affected by changes in pressure and opposing flow velocity and is the length scale for heat transfer both normal and parallel to the fuel surface, so it has an effect on the size and the structure of the flame but not on V_f.

At high opposing flow velocity, however, the gas-phase kinetics can no longer be considered infinitely fast compared to the residence time of the oxidizer at the flame leading edge, and the spread rate becomes dependent on the flow velocity; this dependence has been experimentally correlated with the Damkohler number (Fernandez-Pello et al., 1981), the ratio of the characteristic residence time to the characteristic gas-phase combustion time. Although both the gas-phase residence time, $t_{res} \equiv L_g/V_r = \lambda_g/\rho_g C_g V_r^2$, and the chemical time for second-order kinetics, $t_{comb} \approx L_g^2\rho_g m_f/B_g\rho_g^2 m_f m_{ox} e^{-E_g/RT} \propto 1/\rho_g B_g$, are dependent on the ambient pressure through ρ_g, the Damkohler number is independent of pressure for forced-convective opposing flow where V_r is independent of P_∞. Therefore, the spread rate is expected to be insensitive to pressure even when gas-phase kinetics control the flame spread.

For downward flame spread over a thin fuel in a quiescent, normal-gravity environment, the characteristic opposing flow velocity created by buoyancy is $V_r \approx (g\alpha_g(T_f - T_\infty)/T_\infty)^{1/3}$ and can be high enough for the gas-phase kinetic effect to be important. The Damkohler number for this situation is proportional to $P_\infty^{2/3}$. This implies that as ambient pressure increases, the Damkohler number and the spread rate increase as well. This behavior is observed experimentally for an ambient oxygen level of 21 percent (Lastrina et al., 1971). In addition, spread rate has been correlated with a Damkohler number that includes the effect of pressure on the induced flow (Altenkirch et al., 1980).

In a microgravity environment, buoyancy being almost absent, the above-mentioned effect of the ambient pressure is almost nonexistent. Moreover, in a quiescent environment the

Contributed by the Heat Transfer Division for publication in the JOURNAL OF HEAT TRANSFER. Manuscript received by the Heat Transfer Division June 1994; revision received June 1995. Keywords: Combustion, Microgravity Heat Transfer, Radiation. Associate Technical Editor: W. L. Grosshandler.

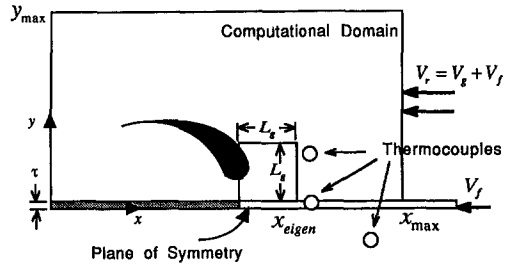

Fig. 1 Schematic of the computational domain and the relative locations of the thermocouples

Damkohler number reaches a maximum as the opposing flow velocity, with respect to the flame, reaches a minimum as $V_r \rightarrow V_f$, assuring fast chemistry. Ambient pressure, therefore, is not expected to influence the spread rate if the model developed for normal-gravity flames remains valid at microgravity. However, at low opposing flow velocity, the quiescent, microgravity configuration being the extreme case, some of the assumptions used in the normal-gravity model are no longer valid. Principal among these is the neglect of radiation.

The importance of radiation can be demonstrated through scaling arguments by comparing the time scales for radiation and conduction heat transfer (Bhattacharjee and Altenkirch, 1992). Radiation and conduction are competing parallel mechanisms for the heat transfer needed for the sensible heating of the fuel preheat zone from T_∞ to T_v. This heating must take place within the solid residence time, $t_{res,s} \equiv L_g/V_f$. The mechanism with a time scale much larger than $t_{res,s}$ clearly is unimportant.

The rate of conductive heat transfer from the gas to the solid is approximately $\lambda_g L_g(T_f - T_v)/L_g$. The heat transfer required for the sensible heating of the fuel is $L_g \rho_s \tau C_s(T_v - T_\infty)$. The conduction time scale, therefore, is: $t_{cond} \sim L_g \tau / F\alpha_s$ where $F \equiv \lambda_g(T_f - T_v)/\lambda_s(T_v - T_\infty)$. The dimensionless number FL_g/τ, the ratio of gas-phase conduction to the solid-phase forward conduction (Altenkirch and Bhattacharjee, 1990), has a value much greater than unity for thin fuels and establishes gas-phase conduction as dominant over solid-phase conduction. When the radiation time scale is large, $R_c \equiv t_{res,s}/t_{cond} = 1$ yields the heat-transfer-limited expression for V_f obtained previously. At high opposing velocity or at normal gravity, V_r is too large and hence L_g is too small for radiation, as we shall see, to have much significance. However, in the quiescent microgravity environment L_g is larger and radiation may play an important role.

To evaluate the influence of radiation on the flame, the radiation time scales should be compared with the gas-phase residence time because radiation affects the flame mostly through cooling of the gas phase (Bhattacharjee and Altenkirch, 1991). The time scale for surface radiation can be shown to be $t_{sr} = t_{res}/R_s$ where $R_s \equiv [\epsilon\sigma(T_v^4 - T_\infty^4)/\lambda_g(T_f - T_\infty)]L_g = t_{res}/t_{sr}$. And, assuming gray radiation from the gas phase with a Planck mean absorption coefficient of a_P, the time scale for gas-phase radiation is: $t_{gr} \sim t_{res}/R_g$ where $R_g \equiv [4a_P\sigma(T_f^4 - T_\infty^4)/\lambda_g(T_f - T_\infty)]L_g^2 = t_{res}/t_{gr}$ (Bhattacharjee and Altenkirch, 1992).

An increase in the ambient pressure P_∞ causes the conduction length scale L_g, and hence R_s, to decrease, thus diminishing the importance of radiation. The Planck mean absorption coefficient, a_P, on the other hand, increases with an increase in P_∞. It is, therefore, difficult to predict whether gas radiation effects will increase or decrease with an increase in P_∞ (Bhattacharjee et al., 1991).

Nomenclature

a_P = Planck mean absorption coefficient (see Table 2), m^{-1}
B_s = pre-exponential factor for pyrolysis = 7.8×10^{16} s^{-1}
B_g = pre-exponential factor for gas-phase reaction = 1.58×10^{11} $m^3/kg \cdot s$
C_g = gas specific heat = 1.465 kJ/kg·K
C_s = solid specific heat = 1.256 kJ/kg·K
E_s = pyrolysis activation energy = 2.494×10^5 kJ/kmol
E_g = combustion activation energy = 1.167×10^5 kJ/kmol
F = flame constant = $\lambda_g(T_f - T_v)/\lambda_s(T_v - T_\infty)$
f = fraction of gas-phase radiation directed to the solid surface (see Table 2)
g = acceleration due to gravity = 9.81 m/s^2
L_v^o = latent heat of vaporization = 368.45 kJ/kg
L_g = reference thermal length = α_g/V_r (see Table 2), m
L_{hd} = flame hang distance, m
L_{ph} = solid preheat length = $(T_v - T_\infty)/|dT_s/dx|_{max}$ (see Table 2), m
L_{py} = length of pyrolysis zone, m
M = molecular weight of the gas mixture, 30 kg/kmol
$m_{ox,\infty}$ = ambient oxygen mass fraction
$\dot{m}''$ = mass flux, kg/m^2
P = pressure, N/m^2
Pr = Prandtl number, variable
P_∞ = ambient pressure = 101, 152, and 203 kPa
$\dot{Q}$ = total gas radiation, W
$\dot{q}''$ = heat flux, kW/m^2
R = universal gas constant = 8.314 kJ/kmol·K
R_c = conduction number = $t_{res,s}/t_{cond}$
R_g = gas radiation number = t_{res}/t_{gr}
R_s = surface radiation number = t_{res}/t_{sr}
$R(x)$ = distribution function for gas-to-surface radiation
S = source term in the conservation equation, appropriate units
s = stoichiometric ratio of cellulose ($C_6H_{10}O_5$) combustion = 1.185
T = temperature, K
T_s = solid temperature, K
T_v = solid vaporization temperature, the first maximum after the preheat zone, K
T_∞ = ambient temperature = 298 K
t = time, s
u, v = x and y velocity, m/s
V_f = absolute value of flame spread rate, m/s
V_g = absolute value of gas velocity, m/s
V_r = reference velocity = $V_g + V_f$, m/s
V_w = blowing velocity, m/s
w = width of the sample, 0.03 m
x, y = coordinate axis, m (origin shown in Fig. 1)
x_{max} = upstream boundary location of the computational domain = $6L_g$, m
x_{min} = downstream boundary location of the computational domain = $-10L_g$, m
y_{max} = top boundary location above the fuel surface = $10L_g$, m
α, ϵ = surface absorptance and emittance, 0.5
α = reference thermal diffusivity, m^2/s
Γ = generic diffusion coefficient for ϕ
ΔH_c = heat of combustion for cellulose = 16.74 MJ/kg
λ = thermal conductivity = 0.0542 W/m·K at 750 K
μ = dynamic viscosity = 2.59×10^{-5} N/m·s at 750 K
ρ = gas density = $MP_\infty/(RT)$, kg/m^3
ρ_s = fuel density, kg/m^3
$\rho_{s,\infty}$ = 519 kg/m^3
σ = Stefan–Boltzmann constant = 5.67×10^{-8} $W/m^2 \cdot K^4$
τ = half-thickness of fuel = 0.0825 mm
ϕ = generic conserved property

Data from a computational model and experiment will be used to show that the importance of the reduction in L_g outweighs the increase in a_p, and the gas-phase radiation effect actually diminishes with an increasing ambient pressure. Computational studies (Bhattacharjee and Altenkirch, 1991, 1992) have shown that radiation, both surface and gas, acts primarily as a cooling mechanism for the flame, thereby slowing flame spread and causing the flame to shrink in size. Therefore, with an increase in P_∞ it is expected that the flame temperature, flame size, and the spread rate will all increase as radiative effects are diminished in microgravity.

Here results of three flame spread experiments conducted aboard the Space Shuttle at three different ambient pressures are compared to computational results in order to explore the strengths and weaknesses of the arguments given above concerning the importance of radiation in flame spreading and ultimately in issues of spacecraft fire safety. The numerical model and experimental data for a single pressure have been presented elsewhere (Bhattacharjee and Altenkirch, 1992). Here, we examine additional data and apply an advanced version of the model that includes radiation coupling between the gas and the solid phase to analyze and interpret the set of experiments in order to gain insight into the effect of ambient pressure on flame spread in a quiescent, microgravity environment.

Mathematical Model

Details of the mathematical model can be found elsewhere (Bhattacharjee and Altenkirch, 1992), so only a summary is presented here for completeness. The model consists of the two-dimensional, steady-state continuity, momentum, species, and energy equations in the gas and the continuity and energy equations in the solid. In addition to the unknown field variables, a boundary condition, V_f, is the desired unknown eigenvalue. The gas-phase equations can be expressed in the common form:

$$\frac{\partial}{\partial x}(\rho u\phi) + \frac{\partial}{\partial y}(\rho v\phi) = \frac{\partial}{\partial x}\left(\Gamma_\phi \frac{\partial \phi}{\partial x}\right) + \frac{\partial}{\partial y}\left(\Gamma_\phi \frac{\partial \phi}{\partial y}\right) + S_\phi \quad (1)$$

where the meanings of ϕ, Γ_ϕ, and the source term S_ϕ are given in Table 1.

Second-order Arrhenius kinetics are used for the fuel and oxygen source terms assuming a one-step, irreversible reaction. The thin-gas emission approximation is used in modeling the radiation from the gas. However, the overall mean Planck absorption coefficient is calculated from a model that ensures an overall radiation energy balance based on a more accurate solution of the radiation transport equation that accounts for total emission and absorption by CO_2 and H_2O in a nonhomogeneous medium and neglects radiation from soot and fuel vapor (Bhattacharjee and Altenkirch, 1991). The perfect gas law is used for the equation of state, and μ is allowed to vary with a square-root dependence on temperature. Boundary conditions for the gas-phase equations are (refer to Fig. 1):

Table 1 Conservation equations (see Eq. (1))

Equation	ϕ	Γ_ϕ	S_ϕ
Continuity	1	0	0
x momentum	u	μ	$-\frac{\partial P}{\partial x}$
y momentum	v	μ	$-\frac{\partial P}{\partial y}$
Fuel	m_f	μ/Pr	$-B_g\rho_g^2 m_f m_{ox} e^{-Eg/RT}$
Oxygen	m_{ox}	μ/Pr	sS_f
Nitrogen	m_n	μ/Pr	0
Energy	C_pT	μ/Pr	$\{-\Delta H_c S_f - 4a_p\sigma(T^4 - T_\infty^4)\}/C_P$

at

$$x = x_{\max}, \quad \phi = \phi_\infty (u_\infty = -V_f, v_\infty = 0)$$

at

$$x = 0, \quad \partial\phi/\partial x = 0, \quad P = P_\infty$$

at

$$y = y_{\max}, \quad \phi = \phi_\infty (\text{for all } \phi \text{ except } v)$$
$$\partial v/\partial y = 0, \quad P = P_\infty$$

at

$$y = 0, \quad u = -V_f, \quad v = V_w, \quad T = T_s$$
$$\text{and for all other } \phi\text{'s} \quad (\rho_g v\phi - \Gamma_\phi \partial\phi/\partial y)_{y=0} = I_\phi$$

where $I_\phi = \dot{m}''$ for fuel and = 0 for oxygen and nitrogen.

The interfacial quantities V_w, T_s, $\dot{m}''$ and V_f are obtained by solving the solid-phase continuity and energy equations:

Continuity:

$$\dot{m}'' = \frac{d}{dx}(\rho_s \tau V_f) \quad (2)$$

Pyrolysis:

$$\dot{m}'' = A_s \rho_s \tau e^{-E_s/RT_s} \quad (3)$$

Energy:

$$\dot{q}''_{\text{gsc}} + \alpha(\dot{q}''_{\text{gsr}} - \dot{q}''_{\text{ser}}) = -\rho_s \tau V_f C_s \frac{dT_s}{dx} + \dot{m}''[L_v^0 + (C_g - C_s)(T_s - T_\infty)] \quad (4)$$

The boundary conditions for these first-order differential equations are $T_s = T_{s,\infty}$ and $\rho_s = \rho_{s,\infty}$ at $x = x_{\max}$. The conduction flux terms from the gas to the solid, $\dot{q}''_{\text{gsc}}$, can be directly obtained from the gas-phase temperature field. The radiative term, following the simplified scheme developed by Bhattacharjee and Altenkirch (1991), is given by:

$$\dot{q}''_{\text{gsr}} = fR(x)\dot{Q}_{gr} \quad (5)$$

$$\dot{Q}_{gr} \equiv 4a_p\sigma w \iint_{\text{Comp.Domain}} (T^4 - T_\infty^4)\,dx\,dy \quad (6)$$

Nomenclature (cont.)

Subscripts/Superscripts

a = accurate
c = combustion
cond = conduction
f = fuel, flame
g = gas phase
gr = gas radiation
gsc = gas-to-surface conduction
gsr = gas-to-surface radiation
n = nitrogen
ox = oxygen
res = residence
sr = surface radiation
ser = surface-to-environment reradiation
s = solid fuel
v = vaporization
∞ = ambient condition
ϕ = pertaining to conserved variable ϕ

which can be obtained from the gas-phase temperature field if the radiation parameters f, the fraction of radiation directed to the surface, $R(x)$, the distribution of gas-to-surface radiation, and a_p are known. These parameters are obtained from the interim solution for the gas-phase field variables using advanced radiation routines and updated as the solution progresses to convergence. The parameters are obtained from a few overall quantities calculated using the accurate solution of the radiative transfer equation:

$$f \equiv \frac{\dot{Q}_{\text{gsr},a}}{\dot{Q}_{gr,a}}; \quad R(x) \equiv \frac{\dot{q}'_{\text{gsr},a}}{\dot{Q}_{\text{gsr},a}}$$

$$a_P \equiv \frac{\dot{Q}_{gr,a}}{4\sigma w \iint_{\text{Comp.Domain}} (T^4 - T_\infty^4)dxdy} \tag{7}$$

The inherent three dimensionality of radiation is introduced into these parameters by considering all possible lines of sight while calculating the radiative flux at the boundary of the computational "box" from which the accurate quantities $\dot{Q}_{gr,a}$, $\dot{Q}_{gsr,a}$, and $\dot{q}'_{\text{gsr},a}$ are evaluated. Although the hydrodynamic model is two dimensional, the effect of the radiative side losses from the flame is taken into account in a simplified manner by equating the width of the radiation "box" to the sample width w.

To close the formulation, one more condition is needed, which is a matching of the surface temperature distribution computed from each phase. This matching is facilitated by fixing the surface temperature, T_{eigen} ($T_\infty < T_{\text{eigen}} < T_v$), at a given location, x_{eigen}, within the computational domain (see Fig. 1). It should be stressed here that the choice of T_{eigen} is arbitrary and has no effect on the solution other than to control the location of the flame leading edge with respect to the boundaries. A suitable choice of T_{eigen} and x_{eigen} assures that the flame occupies the central region of the computational domain.

The solution is started with a guessed gas-phase field, radiation parameters, and boundary conditions. After about 10 iterations of the gas-phase equations, the heat flux from the gas to the solid is computed, and the solid-phase equations are solved to obtain V_f and improved interface conditions. The process is repeated for a few cycles after which the radiation parameters, a_P, f, and $R(x)$ are computed from the gas-phase solution. The gas–solid cycle is restarted with the new radiation parameters, and the entire process is repeated until convergence is obtained for all unknown variables including the radiation parameters.

The surface radiation properties are chosen as: $\alpha = \epsilon = 0.5$ in the absence of any available measurements, and the values of the pyrolysis constants were chosen based on an extensive study (Bhattacharjee et al., 1994a, b) of the first-order Arrhenius kinetics model with regard to flame spread pyrolysis. Other properties are the same as those used before (Bhattacharjee and Altenkirch, 1991).

Experimental

A detailed discussion of the experimental techniques and apparatus, and the experimental data for 1.5 atm, has been pre-

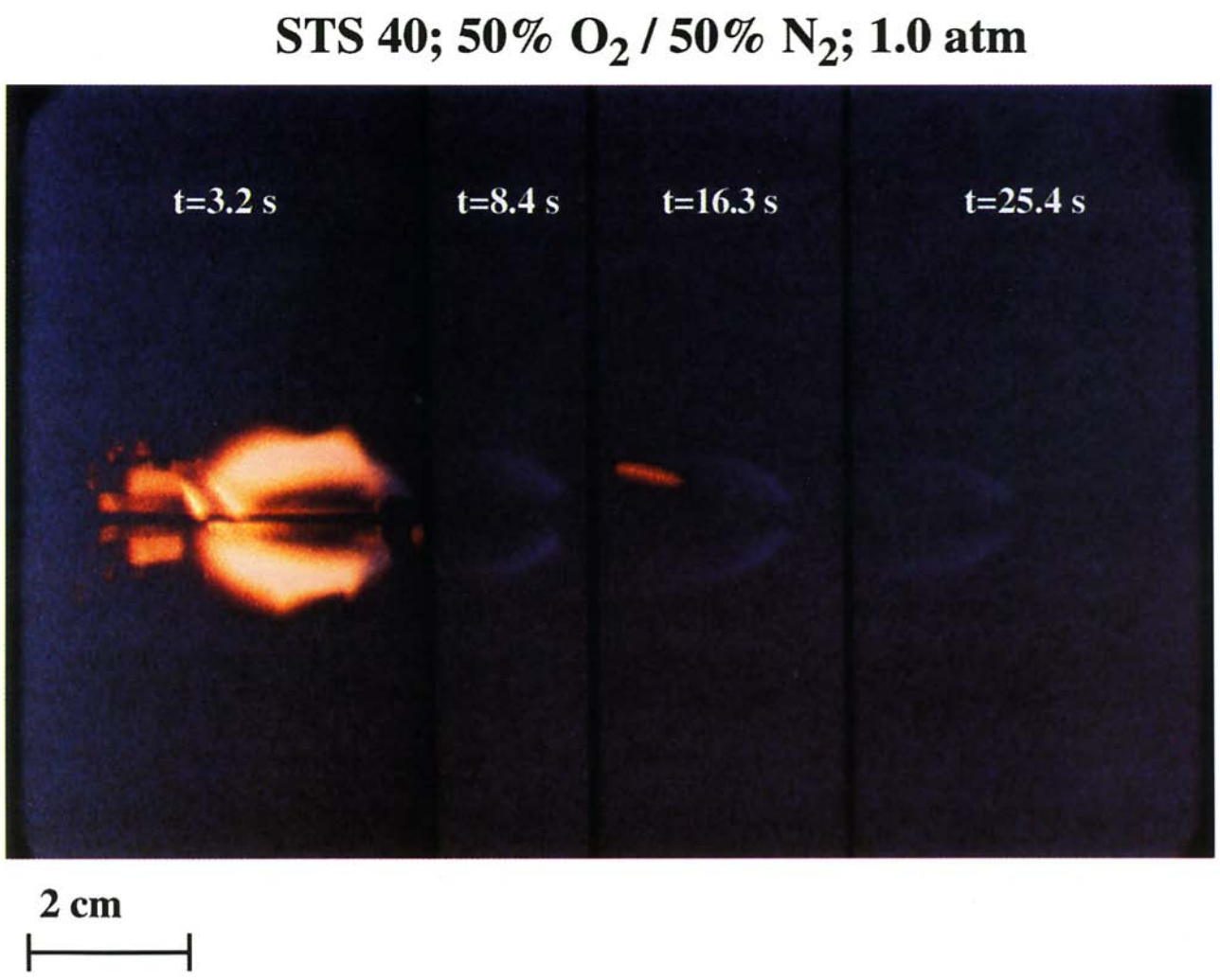

Fig. 2(*a*)

sented elsewhere (Bhattacharjee et al., 1993). The 1.5 atm data are used here as a part of a set of data in which the effects of pressure have been investigated. The experiment is conducted in a sealed chamber filled with a 50/50 (volumetric) oxygen/nitrogen mixture. The test specimen, ashless filter paper, 0.165 mm full thickness, 10 cm long, and 3 cm wide, is ignited at one end, and the resulting flame spread in the quiescent environment is filmed. Three Pt/Pt-Rh thermocouples, one imbedded in the solid and two in the gas phase (Fig. 1), record a time–temperature history as the flame moves past them.

The rate of spread of the flame leading edge, obtained by analyzing the film, is steady. The time–temperature trace from the thermocouples is mapped (Bhattacharjee et al., 1991) into $x-T$ data using this measured spread rate. These data can be used in conjunction with Eqs. (2), (3), and (4) to determine a solid density profile and a net heat flux to the solid for comparison to the complete computational model and the gas-to-surface conduction, which can be calculated from the thermocouple measurements. The implications of measurement uncertainties and thermocouple corrections, which have not been applied here, are discussed elsewhere (Bhattacharjee et al., 1993), the conclusion being that thermocouple corrections, which are difficult to determine accurately, are not particularly significant to the major findings, which are based on differences between measured temperatures.

Results and Discussion

Side-view photographs of the flames at two different ambient pressures are shown in Fig. 2(a) (1.0 atm) and Fig. 2(b) (1.5 atm). The flames, spreading from left to right in the photographs, are symmetric about the fuel surface, which is along $y = 0$. Four frames from the film are shown for each pressure. The times shown on the photographs are the times following the first appearance of a flamelike image on the film. Each flame has a blue leading edge, which for the higher pressure is followed by a long yellow zone, indicative of the presence of soot. The orange glow at the left of the third photograph in Fig. 2(a) is from a portion of a gas-phase thermocouple. The thermocouple is visible in the second photograph in Fig. 2(b).

Temperature contours computed with and without radiation in the theory are shown in Fig. 3. Only one-half of the flame is computed because the problem is symmetric about the fuel half thickness. The origin in the computed flames is the eigen location (where the surface temperature reaches a value of $T_{eigen} = 360$ K). Clearly, the experimental flame shape compares more favorably with the theoretical temperature contours when radiation is included in the model.

Without radiative loss, the maximum gas-phase temperature is about 3680 K, almost the same as the adiabatic, stoichiometric flame temperature, and remains practically unchanged with pressure. The size of the computational flame, defined by the size of

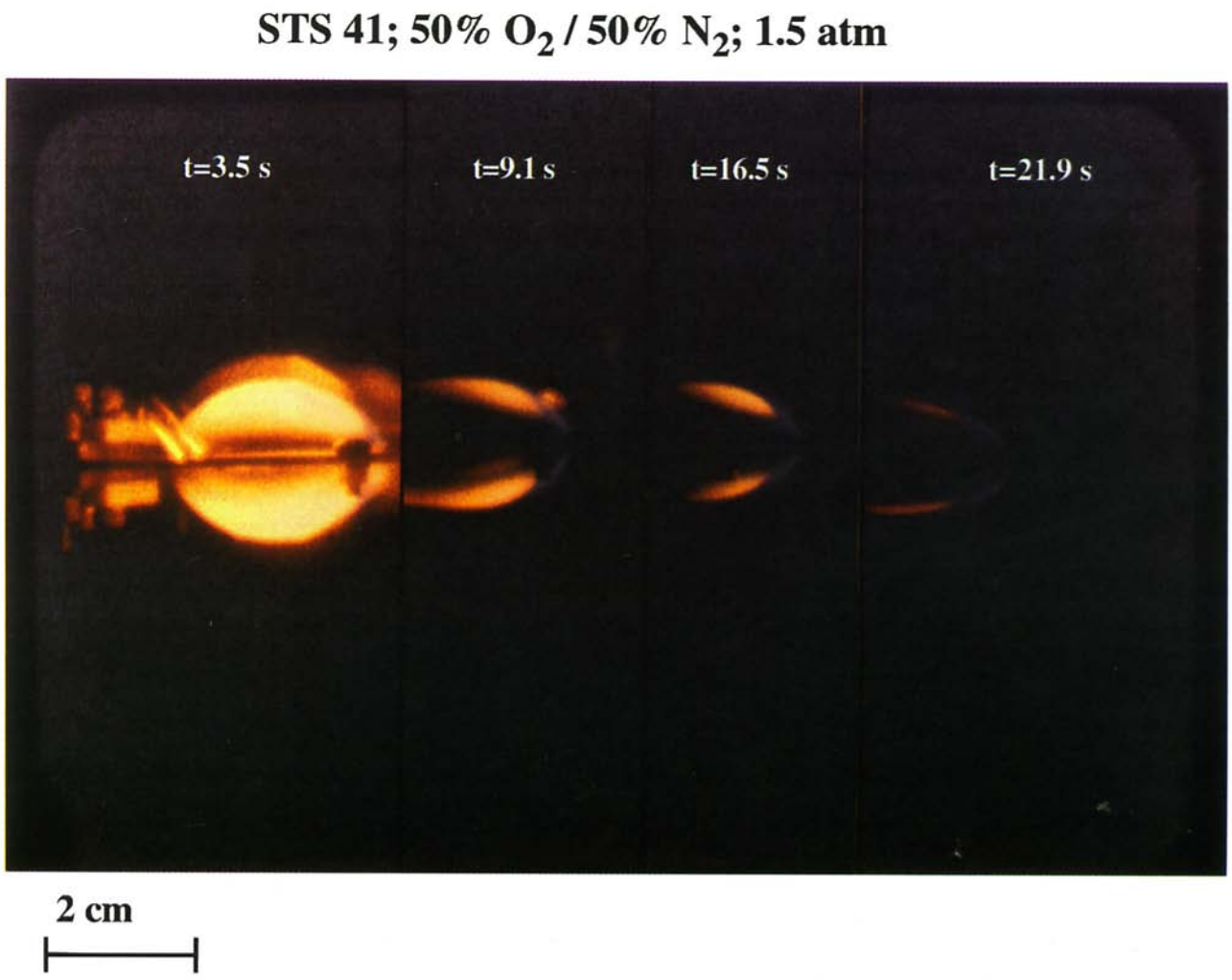

Fig. 2(*b*)

Fig. 2 Side-view photographs of the flames at: (*a*) 1.0 atm, and (*b*) 1.5 atm

the smallest (hottest) temperature contour, is too large to be contained within the domain of the plot and is unrealistic when compared with the flame size seen from the experiment (Fig. 2). As the pressure increases, the flame size in Fig. 3 decreases, and the contours become more and more closely spaced. This behavior can be explained because the length scale, L_g, is inversely proportional to P_∞. Without radiation the computed flame structure should scale with L_g. When the results in Fig. 3 without radiation are replotted in coordinates normalized by L_g, the temperature contours for the different pressures become almost identical as shown in Fig. 4. The contours are not exactly identical because the vaporization temperature depends slightly on P_∞ (Bhattacharjee et al., 1992). Because $L_g \equiv \alpha_g/V_f$ in the quiescent environment, Fig. 4 establishes the spread rate as the reference velocity of the problem if radiation is neglected.

When gas radiation is included in the theory, the peak flame temperature decreases substantially due to radiative cooling, by almost 2000 K, reducing the flame size to something more realistic. However, the hottest contour, the 1200 K line (the inner contour) in Fig. 3, grows in size as P_∞ increases. The increase in size of the computed high temperature region (which will be called the hot zone) with pressure requires some explanation.

At first the slight increase in the size of the hot zone with pressure appears counter-intuitive because L_g, the diffusion length scale, decreases with increasing P_∞ (see Table 3). In fact, the spacing between contours (Fig. 3*b*) decreases, and the low-temperature contour ($T = 1.5T_\infty$) shrinks in size with increasing pressure consistent with a reduction of L_g. But, as the length scale decreases, so does the characteristic optical depth of the flame, defined as $a_P L_g$ (see Table 2); therefore, the radiation loss can be expected to be less severe at higher pressure. Because the radiation loss affects the hottest zone of the flame the most, the high-temperature contour ($T/T_\infty = 4.0$ in Fig. 3*b*) suffers the most shrinkage at the lowest pressure. The maximum gas temperature, therefore, increases with an increase in P_∞ in Table 2. The flame size, identified with the high-temperature contours (the fuel reactivity contours follow almost the same pattern), is therefore expected to increase slightly with an increase in pressure.

The effect of pressure on flame size is not particularly evident from the visible photographs of the flame in Fig. 2; a side-view photograph at $P_\infty = 2$ atm is not available. The gas temperature recorded by the thermocouple 7 mm from the surface is shown for the three different pressures in Fig. 5, and it provides some indirect information on flame size. The temperature increases sharply at $x = 0$, the location of the peak net heat flux, reaches a peak at the flame leading edge, and then decreases before it peaks again at what will be called the flame trailing edge. The distance between these two peaks increases with increasing pressure in Fig. 5 and supports the conclusion that the size of the hot zone increases with increasing pressure. It should be mentioned here that the steady-state assumption has been used in reducing the time–temperature data from the thermocouples. Although the spread rate is very nearly steady, within 0.1 percent, the flame size in terms of the distance between the leading and the trailing edge is observed in the film to increase with time as the flame spreads.

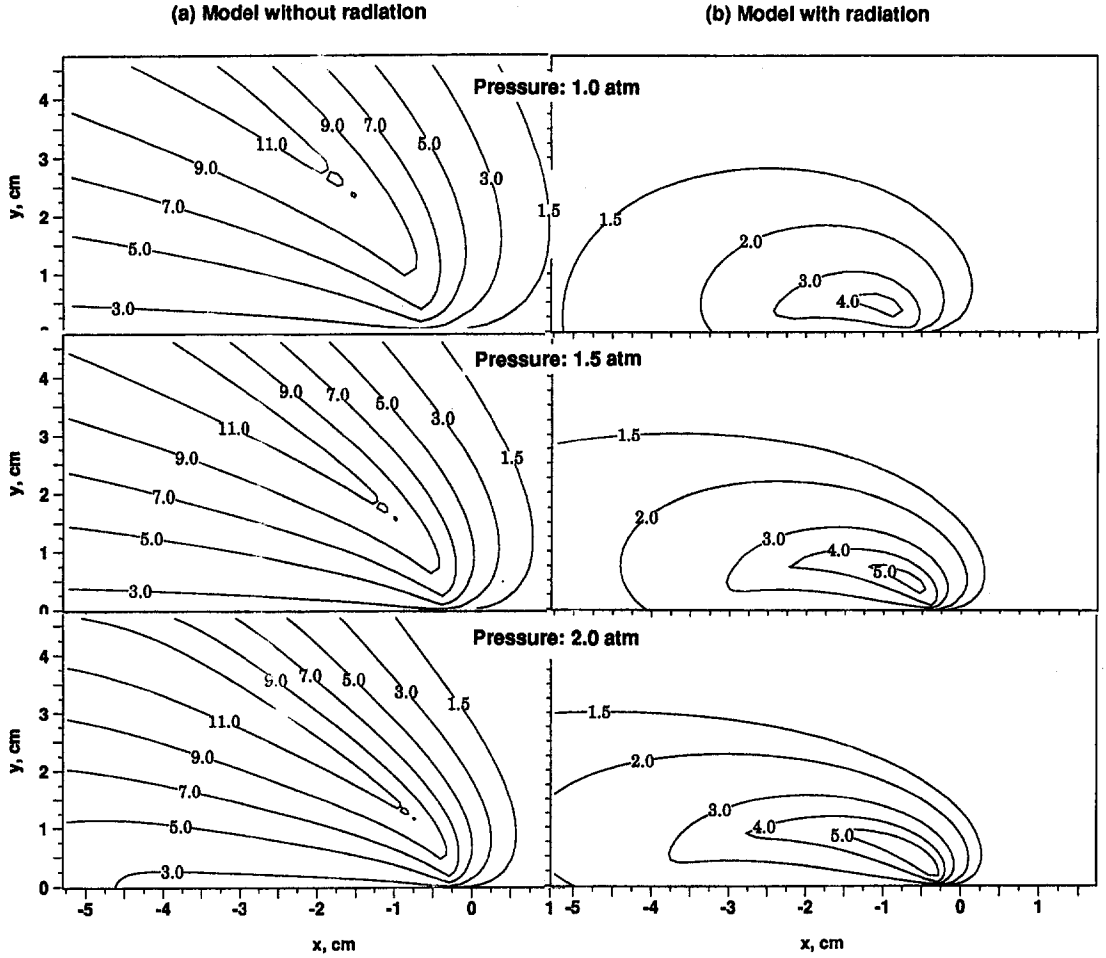

Fig. 3 Temperature contours in units of the ambient temperature 298 K at three different pressures: (a) model without radiation, (b) model with radiation

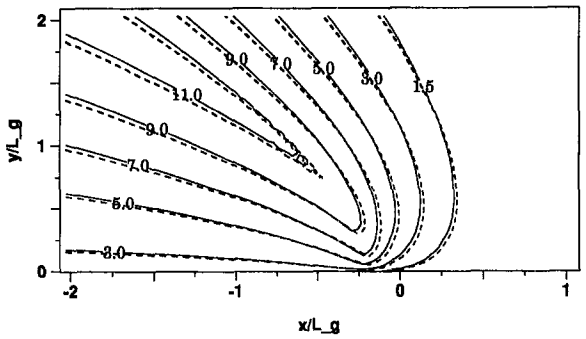

Fig. 4 Temperature contours in dimensionless space

Several important parameters from experiment and three models are summarized in Table 2. In evaluating the spread rate from the de Ris/Delichatsios formula ($V_f = (\pi/4)(\lambda_g/\tau\rho_s C_s)(T_{f,ad} - T_v)/(T_v - T_\infty)$, de Ris, 1969; Delichatsios, 1986), the vaporization temperature T_v is taken to be the maximum surface temperature near the leading edge computed from the non-radiative model. With an increase in ambient pressure, T_v increases slightly (see Table 2), as anticipated from the first-order pyrolysis kinetics (Bhattacharjee et al., 1993), which explains the slight decrease in spread rate in the de Ris and non-radiative models. Note the excellent agreement on V_f, up to one tenth of a mm/s, between the de Ris and the non-radiative model, despite the removal of a number of simplifying assumptions—negligible hang distance, Oseen flow, linearized interface conditions, infinite-rate chemistry, constant vaporization temperature, constant properties—in the latter model. This must be due to canceling effects of different physics, and the fact that λ_g used in the de Ris formula is evaluated at the reference temperature, $(T_{f,ad} + T_\infty)/2$, rather than at T_v. This choice of reference temperature was found to be "fortuitously appropriate" by Wichman and Williams (1983) in correlating the experimental data of Fernandez-Pello et al. (1981) for opposed flow flame spread over thin cellulosic fuel.

The experimental data in Table 2 clearly indicate that the spread rate increases with pressure. Similar behavior has been observed at another oxygen level (Ramachandra et al., 1995). Without radiation, the de Ris/Delichatsios formula as well as the numerical model completely fail to capture this behavior. Moreover, the predicted V_f is about three times larger than the data. When radiation is included in the model, the agreement between model and experiment improves dramatically (to within 10 percent), and the V_f versus P_∞ behavior is correctly captured.

Without radiation, the maximum gas temperature tends toward the adiabatic, stoichiometric temperature ($T_{f,ad} = 3908$ K) in the downstream direction (see Table 2). With the inclusion of radiation in the model, T_f drops precipitously (by almost 2000 K), which must be the reason behind the dramatic decrease of V_f. With an increase in pressure the radiation parameters, a_P and f, understandably increase. However, for reasons already explained, T_f increases and T_v decreases with an increase in P_∞. Even with no radiation feedback, i.e., $f = 0$, in the model, V_f and T_f have been found to increase with P_∞. The increase in T_f with P_∞, therefore, must be responsible for the observed V_f versus P_∞ behavior. The maximum temperature, $T_{\max}$, recorded by the gas-phase thermocouple at $y = 7$ mm (see Fig. 1) first increases and then slightly decreases (see Table 2) with P_∞. Because the flame size changes with P_∞, $T_{\max}$ may not be a good indicator of T_f.

The surface temperature profiles at the three pressures are shown in Fig. 6. The sharp rise in surface temperature near the flame leading edge indicates the preheat zone. The surface temperature soon reaches a plateau as the pyrolysis begins with the maximum temperature defined as the vaporization temperature T_v. The pyrolysis zone follows, where the temperature is moderated by vaporization, the end of this zone being signaled by the rise in temperature of the remaining nonvolatile char.

A number of characteristic lengths of the flame, calculated from the surface temperature profiles, for the experiments and different models are expressed in terms of L_g in Table 3. Results for the de Ris model are obtained for the computational solution, which assumes nonzero flame hang distance, defined below (Bhattacharjee, 1993). In both the de Ris model and non-radiative model, the diffusion length scale is primarily controlled by the ambient pressure because the spread rate (Table 2) remains almost unchanged with pressure in these models. The sevenfold increase in L_g compared to the de Ris model for the non-radiative model is mostly due to the introduction of variable density in the model. An even larger value of L_g is calculated for the experiments and the radiative models because of smaller spread rates.

The characteristic preheat length is defined as $L_{ph} \equiv (T_v - T_\infty)/|dT_s/dx|_{\max}$, where $|dT_s/dx|_{\max}$ is the maximum temperature gradient in the preheat zone, similar to the approach taken to define the flame thickness (Kanury, 1977). An example of the dT_s/dx profile is given in Fig. 7 where the T_s profile is differentiated without any smoothing. If radiation is unimportant, solid heating takes place entirely by means of conduction; hence, L_{ph} is expected to be proportional to the gas-conduction length scale, L_g, as obtains for the de Ris and the non-radiative models. In the experimental results this proportionality is lost

Table 2 A comparison of different parameters at three different pressures

		Pressure (P_∞, atm)		
		1.0	1.5	2.0
Spread rate (V_f, mm/s)	Experiment	3.6	4.5	5.5
	Model			
	de Ris model	11.7	11.5	11.4
	No radiation	11.7	11.5	11.4
	Radiation	3.2	4.9	5.9
Maximum gas temperature* (T_f, K)	Experiment	1343	1386	1367
	Model			
	No radiation	3674	3680	1682
	Radiation	1326	1544	1751
Vaporization temperature (T_v, K)	Experiment	719	743	710
	Model			
	No radiation	749	756	761
	Radiation	728	740	749
Radiation parameters	Planck mean (a_P, m^{-1})	2.7	3.3	4.4
	Percent feedback, f	17%	29%	32%

* Maximum temperature 7 mm from the surface.

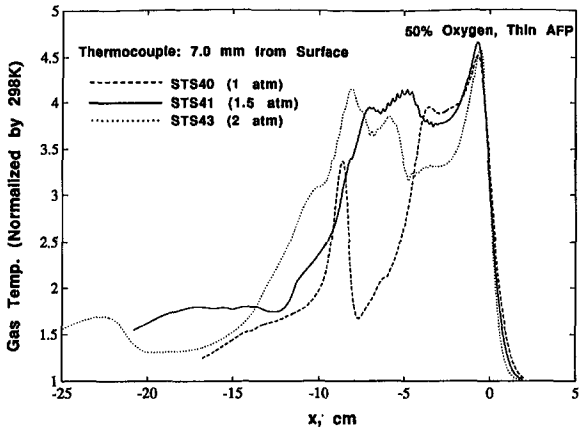

Fig. 5 Measured temperature profiles 7 mm away from the surface at three different ambient pressures

(see Table 3), and the model with radiation captures the experimental trend if not the absolute values. Because radiation acts as a net loss, a reduction in the length scale with the inclusion of radiation can be predicted from a scale analysis (Bhattacharjee et al., 1991).

As will be shown later, the x location, x_{peak}, in the preheat zone where $|dT_s/dx|_{\max}$ occurs is also the location of the peak heat flux from the gas to the solid. This location has been found to be the location of the flame leading edge for infinite-rate chemistry (Bhattacharjee, 1993). The location where pyrolysis starts is defined as the point where T_s reaches its first maximum T_v, and dT_s/dx becomes zero (see Fig. 7). The distance between this location and x_{peak} is defined as the flame hang distance, which is expressed in terms of L_g for different models and experiments in Table 3. The hang distance L_{hd} found in the computed solution of the de Ris model agrees quite well with a correlation established by Bhattacharjee et al. (1994b) that predicts a value of 0.44 L_g under all pressures. However, in the microgravity experiments as well as in the model with radiation, the hang distance increases by three times as the ambient pressure doubles from 1 to 2 atm. It should be mentioned that in the analytical solution for the de Ris spread rate (de Ris, 1969; Delichatsios, 1986) this hang distance was assumed to be zero.

The length of the pyrolysis zone, L_{py}, obtained from the T_s profiles is also listed in Table 3. A sudden change in the slope of the T_s profile is assumed to indicate the completion of the pyrolysis zone. Without radiation, according to a formula developed by Bhattacharjee et al. (1994b), the pyrolysis length, L_{py}, with the properties used in this work, is given as $L_{py} = 5.5\ L_g$ irrespective of the ambient pressure; this is in reasonable agreement with the computed values for non-radiative models. However, in the experiments and in the model with radiation, L_{py}, expressed in the units of L_g, increases dramatically with an increase in pressure (see Table 3). It should be mentioned here that the experimental values have been obtained with the steady-state assumption, which is somewhat questionable for the pyrolysis length.

At the end of the pyrolysis zone (Fig. 6), the temperature increases sharply; this is most likely due to sensible heating of the remaining nonvolatile char. The distance between the two peaks of the surface temperature, therefore, can be interpreted as the distance between the leading and the trailing edges of the gas-phase flame. The changes in temperature beyond the trailing edge of the flame (Figs. 5 and 6) are a result of unsteady glowing combustion of the remaining nonvolatile char, which is evident from the films. The films show that the surface reactions occur mostly near the edges of the sample near the sample holder. The steady-state computational model does not include any exothermic surface reaction, and so no comparison between theory and experiment can be made beyond the completion of the pyrolysis zone.

The net heat flux profiles at the three different pressures, obtained using the procedure briefly described in the experimental section and described in detail elsewhere (Bhattacharjee et al., 1993), are shown in Fig. 8. The location of the peak heat flux has been identified with the location of $|dT_s/dx|_{\max}$ for each experiment. This location, defined as the flame leading edge, is arbitrarily chosen as the origin for each flame in Figs. 5–8. In the downstream (negative x) direction, a second peak can be detected in each profile approximately at the location of the trailing edge. The positive heat flux from the gas to the solid at the trailing edge implies an endothermic process there; if burnout had occurred upstream of this location, the heat flux would be zero because of the symmetry condition. The second peak is probably caused by the trailing edge of the flame, which bends back toward the surface; limited support for this can be seen in the film, although a definitive statement is difficult to make because the flame becomes progressively fainter toward the trailing edge. The distance between these two heat flux peaks, therefore, can be taken as the flame size, which increases with increasing pressure consistent with the conclusion from the model with radiation.

Table 3 A comparison of different length scales at three different pressures

		Pressure (P_∞, atm)		
		1.0	1.5	2.0
Diffusion length scale (mm), L_g	Experiment	98.3	51.7	32.2
	Model			
	de Ris model	4.33	2.92	2.22
	No radiation	30.5	20.6	15.7
	Radiation	114.9	42.8	25.0
Preheat length, L_{ph}	Experiment	0.10 L_g	0.17 L_g	0.24 L_g
	Model			
	de Ris model	0.36 L_g	0.36 L_g	0.36 L_g
	No radiation	0.24 L_g	0.23 L_g	0.22 L_g
	Radiation	0.05 L_g	0.10 L_g	0.14 L_g
Flame hang distance, L_{hd}	Experiment	0.10 L_g	0.18 L_g	0.30 L_g
	Model			
	de Ris model	0.43 L_g	0.43 L_g	0.43 L_g
	No radiation	0.29 L_g	0.28 L_g	0.27 L_g
	Radiation	0.04 L_g	0.10 L_g	0.17 L_g
Pyrolysis length, L_{py}	Experiment	0.04 L_g	0.31 L_g	1.86 L_g
	Model			
	No radiation	2.36 L_g	2.32 L_g	2.28 L_g
	Radiation	0.37 L_g	1.10 L_g	2.50 L_g

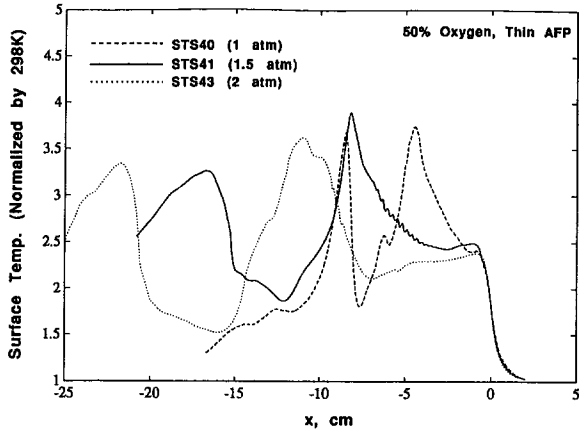

Fig. 6 Measured surface temperature profiles at three different ambient pressures

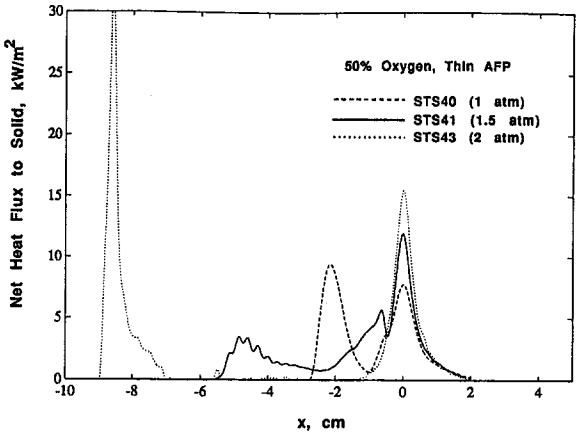

Fig. 8 Net heat flux from the gas to the solid, calculated by solving the solid-phase energy equation from the measured solid temperature

One drawback of the present model is that it does not predict the flame structure at the trailing edge of the flame properly. Several factors are responsible for this, and they have been discussed elsewhere (Bhattacharjee and Altenkirch, 1992). Because flame "reattachment" at the trailing edge has not been observed with the current steady-state model, the net heat flux from the model, shown in Fig. 8, has only one peak that corresponds to the leading edge. Despite difficulties with trailing edge prediction, the dependencies on pressure of the net heat flux and the spread rate (Table 2) seen from the model with radiation are similar to that found in the experiment. This supports the conclusion that the flame spread process in a quiescent, microgravity environment is controlled by the leading edge, as it is in other opposed-flow environments.

Conclusions

The effect of ambient pressure on flame spread over a thin cellulosic fuel in a quiescent, microgravity environment has been studied experimentally and computationally. Experiments were carried out at three different pressures aboard three different Space Shuttle missions. The model includes gas-phase radiation, including the radiation feedback from the gas to the solid. To evaluate the importance of radiation, a set of calculations in which radiation was completely neglected was also presented.

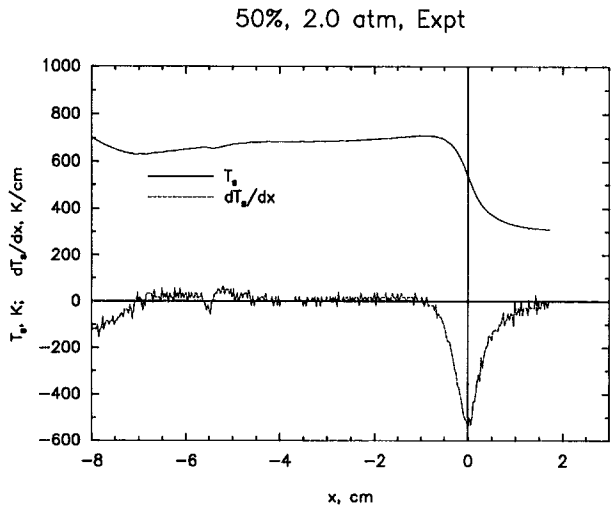

Fig. 7 Measured surface temperature and the corresponding temperature gradient for P_∞ = 2.0 atm

Data indicate that the spread rate increases with increasing pressure. This is contrary to the results expected from the model in which radiation effects are not considered, in which the spread rate is found to be almost independent of pressure. The flame, taken to correspond to the high temperature contours, scales with the diffusion length scale when radiation is neglected, is unrealistically large, and unrealistically hot. When radiation is included, the flame cools substantially and decreases in size. The effect of radiation seems to be more pronounced at lower pressures because the characteristic optical depth of the flame is larger there. Consequently, the flame is cooler and spreads more slowly at lower pressure.

The surface temperature and the gas temperature measurements, and the inferred data on the net heat flux from the gas to the solid surface are all found to be qualitatively consistent with the model including radiation near the leading edge of the flame. The dependence of flame spread rate and various length scales on pressure, which is quite different from what is seen in Earth-bound downward flame spread, is correctly predicted.

Acknowledgments

This work was supported by NASA through Contract No. NAS3-23901. We thank Sandra Olson for serving, for a period of time, as Contract Monitor and Prof. S. V. Patankar for providing to us an initial version of the gas-phase software. We gratefully acknowledge the contributions of Ralph Zavesky, John Koudelka, and the SSCE flight hardware team at the NASA-Lewis Research Center and the program support of NASA Headquarters, Microgravity Division, Office of Space Science and Applications.

References

Altenkirch, R. A., and Bhattacharjee, S., 1990, "Low Gravity Fluid Dynamics and Transport Phenomena," *Progress in Astronautics and Aeronautics,* Vol. 130, pp. 723–740.

Altenkirch, R. A., Eichhorn, R., and Shang, P. C., 1980, *Combustion and Flame,* Vol. 37, pp. 71–83.

Bhattacharjee, S., and Altenkirch, R. A., 1991, *Twenty-Third Symposium (International) on Combustion,* The Combustion Institute, Pittsburgh, PA, pp. 1627–1633.

Bhattacharjee, S., and Altenkirch, R. A., 1992, *Twenty-Fourth Symposium (International) on Combustion,* The Combustion Institute, Pittsburgh, PA, pp. 1669–1676.

Bhattacharjee, S., 1993, *Combustion and Flame,* Vol. 93, pp. 434–444.

Bhattacharjee, S., Altenkirch, R. A., and Sacksteder, K., 1993, *Combustion Science and Technology,* Vol. 91, pp. 225–231.

Bhattacharjee, S., Altenkirch, R. A., Olson, S. L., and Sotos, R. G., 1994a, ASME Journal of Heat Transfer, Vol. 113, pp. 670–676.

Bhattacharjee, S., Bhaskaran, K. K., and Altenkirch, R. A., 1994b, *Combustion Science and Technology,* Vol. 100, pp. 163–183.

Bhattacharjee, S., West, J., and Dockter, S., 1995, "A Simplified Theory for de Ris Flame over Thin and Thick Fuels," *Combustion and Flame,* to appear.

de Ris, J. N., 1969, *Twelfth Symposium (International) on Combustion,* The Combustion Institute, Pittsburgh, PA, p. 241–252.

Delichatsios, M. A., 1986, *Combustion Science and Technology,* Vol. 44, pp. 257–267.

Fernandez-Pello, A. C., Ray, S. R., and Glassman, I., 1981, *Eighteenth Symposium (International) on Combustion,* The Combustion Institute, Pittsburgh, PA, pp. 579–587.

Kanury, M., 1977, *Introduction to Combustion Phenomenon,* Gordon and Breach Science Publishers, New York.

Lastrina, F. A., Magee, R. S., and McAlevy, R. F., 1971, *Thirteenth Symposium (International) on Combustion,* The Combustion Institute, Pittsburgh, PA, pp. 935–948; comments by J. N. de Ris.

Ramachandra, P. A., Altenkirch, R. A., Bhattacharjee, S., Tang, L., Sacksteder, K., and Wolverton, M. K., 1995, *Combustion and Flame,* Vol. 100, pp. 71–84.

Wichman, I. S., and Williams, F. A., 1983, *Combustion Science and Technology,* Vol. 32, pp. 91–123.

Williams, F. A., 1976, *Sixteenth Symposium (International) on Combustion,* The Combustion Institute, Pittsburgh, PA, pp. 1281–1294.